Mechanics of Materials 126 (2018) 75–85

Contents lists available at ScienceDirect

Mechanics of Materials

journal homepage: www.elsevier.com/locate/mechmat

Research paper

A multiscale numerical approach for the finite strains analysis of materials reinforced with helical fibers

Thiago André Carniel[a], Bruno Klahr[a], Eduardo Alberto Fancello[a,b,*]

[a] GRANTE - Department of Mechanical Engineering, Federal University of Santa Catarina, Florianópolis, SC, Brazil
[b] LEBm - University Hospital, Federal University of Santa Catarina, Florianópolis, SC, Brazil

ARTICLE INFO

Keywords:
Multiscale
Homogenization
Finite element method
Tendon
Soft tissue
Helical fiber

ABSTRACT

Present study provides a multiscale numerical approach based on representative volume elements (RVE) for the finite strain analyses of materials reinforced with helical fibers. An RVE with wavy-like boundaries bioinspired in the microstructure of tendon fascicles is proposed. Due to the unusual geometry of the RVE, a non-periodic mesh mapping will likely occur, precluding the numerical implementation of the periodic boundary condition in a straightforward manner. Moreover, it is verified that the others classical boundary conditions, namely, the linear boundary displacements model and the minimally constrained model, seem not to be suitable choices for the multiscale analyses of this class of RVEs. Motivated by these facts, two mixed boundary conditions allying characteristics of both, linear and minimal models, are suggested. The kinematic constraints on the RVE are enforced via variational principles and Lagrange multipliers. A displacement-controlled triaxial test performed on a numerical specimen larger than the RVE is proposed as a reference solution for the multiscale responses of the RVE. A set of numerical results concerning microscopic strain fields and macroscopic stress-stretch curves points out that one of the proposed mixed models predicts with great accuracy not only the homogenized quantities but also the kinematic fields developed within the specimen. The computational homogenization strategy addressed in this manuscript can be extended to other fiber-reinforced materials composed of different fiber arrangements also including dissipative effects. Moreover, the boundaries surfaces of the RVE are not restricted to any particular layout and the finite element mesh do not require particular mappings nor additional algorithmic handling.

1. Introduction

Helical shapes appear in the morphology of several biological structures at different length scales. They can be found from the molecular level – DNA and collagen molecules – to macroscopic structures such as seashells, horns and plant tendrils (Huang and Mei, 2015; Wang et al., 2016). At microscopic scales, wood, bamboo and bone are examples of composite materials that present helical characteristics in their structures (Wang et al., 2016; Palombini et al., 2016). Similarly, helically oriented collagen fibrils are observed within some connective tissues, e.g.: in fascicles of tendons and in the lamella of the cornea (Kalson et al., 2015; Bell et al., 2018). Such microstructural organizations provide tissues with particular biomechanical and physiological behaviors, most of them related to load-bearing reinforcements and mechanotransduction mechanisms (Wang, 2006; Lavagnino et al., 2015).

Among the remarkable physical properties related to this kind of biocomposites, those associated to their mechanical behavior have received particular attention from the scientific community and have been used as inspiration for the design of new structural materials (Sanchez et al., 2005; Huang and Mei, 2015; Wang et al., 2016; Zhang et al., 2016; Kravchenko et al., 2017). For example, seeking for improvements on mechanical properties, new materials composed of helical carbon or polymer fibers have been thoroughly investigated (among others, Ho et al., 2009; Yashima, 2010; Raghubanshi et al., 2016; Deng et al., 2017). In view of the aforementioned facts, the understanding in what ways the helical substructures affect the macroscopic mechanical responses, and *vice-versa*, becomes a relevant subject to both analysis and material design.

Computational multiscale approaches based on the homogenization of representative volume elements (RVE) provide an appealing framework to investigate the macro and micro mechanical behavior of this class of materials (Blanco et al., 2014; de Souza Neto et al., 2015). In this RVE-based theories, the classically used multiscale boundary conditions are the linear boundary displacements model, the periodic

* Corresponding author.
E-mail address: eduardo.fancello@ufsc.br (E.A. Fancello).

https://doi.org/10.1016/j.mechmat.2018.07.014
Received 6 April 2018; Received in revised form 19 July 2018; Accepted 25 July 2018
Available online 01 August 2018

boundary displacements model and the minimally constrained model, also known as the uniform traction model (de Souza Neto et al., 2015). However, to the best of the authors' knowledge, previous works with similar approach in this field are restricted to small strains (Messager and Cartraud, 2008; Frikha et al., 2013), not covering a wide set of cases in which this kinematic assumption is not supported (e.g., fibrous soft tissues).

Based on this, the present work extends these efforts providing a multiscale approach at finite strains for the numerical analysis of RVEs composed of helical fibers. The microstructural equilibrium is cast within a variational principle and the kinematic constraints are enforced with the aid of Lagrange multipliers (Miehe, 2003). Moreover, the material phases of the RVE can be modeled within a variational constitutive framework for general dissipative materials (Ortiz and Stainier, 1999; Radovitzky and Ortiz, 1999).

Aiming at multiscale analyses of tendon tissues, an RVE bioinspired in the microstructure of tendon fascicles is proposed. Briefly, tendon fascicles are mainly composed of helical arrangements of bundles of collagen fibrils, called collagen fibers, surrounded by tenocyte cells (cellular matrix) (Kalson et al., 2015). Based on this morphology, RVEs with helical (wavy-like) boundaries are required to account for the important continuity of the fibers. Accordingly, due to the unusual shape of the resulting RVE, the mesh generation must be able to provide a consistent one-to-one mapping between nodes of the periodic boundaries. On the other hand, if a non-periodic mesh is achieved, weak approaches could be employed instead (Nguyen et al., 2012). However, the numerical implementation of such approaches into a conventional nonlinear finite element code is not straightforward. Moreover, it was verified that the linear and minimal models are not suitable choices for multiscale numerical analyses of this unusual RVEs. On the other hand, mixed types of multiscale boundary conditions seem to be a convenient alternative to the classical models. Generally, these boundary conditions mix two types of the classical ones, where several combinations are possible (see the works of Hazanov and Amieur, 1995; Pahr and Zysset, 2008; Mercer et al., 2015, for example).

Motivated by these facts, the main contribution of this manuscript is to propose an appropriate boundary condition capable to predict not only the macroscopic (homogenized) quantities but also the kinematic fields developed within the RVE. Therefore, two mixed boundary conditions allying characteristics of the linear and minimal models are suggested. A numerical strategy based on a displacement-controlled triaxial test is proposed to verify the ability of such models to predict the multiscale responses. In this case, homogenized stress-stretch curves and strains fields developed on the RVE are investigated.

This manuscript is organized as follows. Section 2 describes the theoretical and numerical methods employed in this work. An overview of the multiscale theory at finite strains is shown in Section 2.1. Section 2.2 addresses details about the proposed multiscale boundary conditions and the solution strategy used. The numerical protocol employed to verify the ability of the proposed boundary conditions and related multiscale approach are shown in Section 2.3. Results are reported in Section 3 and discussed in Section 4. Conclusions of the main achievements are listed in Section 5. Finally, further technical details related to numerical implementations within a conventional nonlinear finite element code are provided in the appendices.

2. Methods

2.1. Multiscale theory at finite strains

This section addresses the fundamental principles of a multiscale theory based on RVEs and formulated in a variational framework at finite strains. This approach leads to a class of multiscale models extensively discussed by many authors (among others, Miehe et al., 2002; Miehe, 2003; Blanco et al., 2014; de Souza Neto et al., 2015; Saeb et al., 2016) and its theoretical basis relies on two main concepts: kinematic admissibility and energetic consistency between the macro and micro scales.

2.1.1. Kinematic admissibility

In the present multiscale theory, the displacement $\mathbf{u}(\mathbf{X})$ and the deformation gradient $\mathbf{F} \overset{\text{def}}{=} \mathbf{I} + \nabla_{\mathbf{X}}\mathbf{u}$ at a macroscopic point $\mathbf{X}$ are related to theirs respective microscopic fields $\mathbf{u}_\mu(\mathbf{Y})$ and $\mathbf{F}_\mu \overset{\text{def}}{=} \mathbf{I} + \nabla_{\mathbf{Y}}\mathbf{u}_\mu$ through the following equations:

$$\mathbf{u} - \langle \mathbf{u}_\mu \rangle = \mathbf{0}, \quad \mathbf{F} - \langle \mathbf{F}_\mu \rangle = \mathbf{0}, \tag{1}$$

where the notation

$$\langle (\cdot) \rangle \overset{\text{def}}{=} \frac{1}{V_\mu} \int_{\Omega_{\mathbf{Y}}} (\cdot)\, \mathrm{d}V_\mu, \tag{2}$$

represents the volumetric average of the quantity $(\cdot)$ and V_μ is the volume of the RVE in the referential (undeformed) domain $\Omega_{\mathbf{Y}}$ with boundaries $\Gamma_{\mathbf{Y}}$. The mapping defined in (2) is usually known as homogenization, being this nomenclature adopted in this manuscript.

In this theory, equations (1) represent constraints on the microscopic displacement field, preventing translational and rotational rigid body motions of the RVE, respectively. Based on this, only the microscopic fields $\mathbf{u}_\mu$ that respect the postulates (1) are kinematically admissible, motivating the definition of the so-called minimal space of kinematically admissible microscopic displacements $\mathcal{K}^{\min}_{\mathbf{u}_\mu}$, which is formally denoted as

$$\mathcal{K}^{\min}_{\mathbf{u}_\mu} \overset{\text{def}}{=} \{\mathbf{u}_\mu | \mathbf{F} - \langle \mathbf{F}_\mu \rangle = \mathbf{0};\ \mathbf{u} - \langle \mathbf{u}_\mu \rangle = \mathbf{0}; \quad \forall\ \mathbf{Y} \in \Omega_{\mathbf{Y}}\}. \tag{3}$$

In view of (3), the corresponding minimal virtual space $\mathcal{V}^{\min}_{\mathbf{u}_\mu}$ can be defined as

$$\mathcal{V}^{\min}_{\mathbf{u}_\mu} \overset{\text{def}}{=} \left\{ \mathbf{w} = \mathbf{w}_1 - \mathbf{w}_2 \,\middle|\, \mathbf{w}_1, \mathbf{w}_2 \in \mathcal{K}^{\min}_{\mathbf{u}_\mu} \right\}. \tag{4}$$

A fundamental assumption in this class of theories relies on the expansion of the microscopic displacement field in the form

$$\mathbf{u}_\mu \overset{\text{def}}{=} \mathbf{u} + (\nabla_{\mathbf{X}}\mathbf{u})\mathbf{Y} + \tilde{\mathbf{u}}_\mu, \tag{5}$$

in which $\mathbf{u}$ is a constant part, $(\nabla_{\mathbf{X}}\mathbf{u})\mathbf{Y}$ is a linear contribution and $\tilde{\mathbf{u}}_\mu$ is the displacement fluctuation field of the RVE, representing a high order term.

Taking the expansion (5) into account, Blanco et al. (2014) and de Souza Neto et al. (2015) redefine the space (4) in terms of the variations $\mathrm{d}\tilde{\mathbf{u}}_\mu$ of the fluctuation field, and by rephrasing the classical Hill-Mandel Principle of macro-homogeneity, they frame this multiscale theory into an elegant variational structure. In this case, the aforementioned authors show that the stress homogenization and the microscopic equilibrium equation are derived without *a priori* assumptions, as will be presented in the sequence.

It is important to mention that, since no inertial effects are considered in this work, the macroscopic displacement $\mathbf{u}$ in (3) is set to zero (see de Souza Neto et al., 2015 for further details on inertial effects in multiscale analyses). This assumption will be considered henceforward.

2.1.2. The principle of the multiscale virtual work

The energetic consistency between the macro and micro scales is established by the principle of the multiscale virtual work

$$\mathbf{P} : \mathrm{d}\mathbf{F} = \langle \mathbf{P}_\mu : \mathrm{d}\mathbf{F}_\mu \rangle, \qquad \forall\ \mathrm{d}\mathbf{u}_\mu \in \mathcal{V}_{\mathbf{u}_\mu}, \tag{6}$$

that represents a variational statement of the Hill-Mandel principle (Blanco et al., 2014; de Souza Neto et al., 2015). The second order tensors $\mathbf{P}$ and $\mathbf{P}_\mu$ are the macroscopic and microscopic first Piola-Kirchhoff stresses, respectively. In Equation (6), the variational space

$$\mathcal{V}_{\mathbf{u}_\mu} \overset{\text{def}}{=} \{\mathbf{w} = \mathbf{w}_1 - \mathbf{w}_2 | \mathbf{w}_1, \mathbf{w}_2 \in \mathcal{K}_{\mathbf{u}_\mu}\} \tag{7}$$

is defined, which depends on a proper space $\mathcal{K}_{\mathbf{u}_\mu}$. The space $\mathcal{K}_{\mathbf{u}_\mu}$ is a

kinematically admissible space that represents a set of multiscale models (microscopic boundary conditions) according to the level of imposed kinematic constraints on the RVE. In other words, any space $\mathcal{K}_{\mathbf{u}_\mu} \subset \mathcal{K}^{\min}_{\mathbf{u}_\mu}$ that satisfies the variational statement (6) defines an admissible deformation field of the RVE. Among the broad range of admissible spaces $\mathcal{K}_{\mathbf{u}_\mu}$, the classical multiscale boundary conditions widely mentioned in literature are the following: the Taylor model (rule of mixtures); the periodic boundary displacements model; the linear boundary displacements model; the minimally constrained model, also known as the uniform traction model (de Souza Neto et al., 2015). Particularly, the minimally constrained model is represented by the space (3) and the linear boundary displacements model is formally defined as

$$\mathcal{K}^{\text{lin}}_{\mathbf{u}_\mu} \overset{\text{def}}{=} \left\{ \mathbf{u}_\mu \in \mathcal{K}^{\min}_{\mathbf{u}_\mu} \,\middle|\, \mathbf{u}_\mu = (\nabla_{\mathbf{X}}\mathbf{u})\mathbf{Y}; \quad \forall\ \mathbf{Y} \in \Gamma_{\mathbf{Y}} \right\}. \tag{8}$$

Finally, one can show that the stress homogenization

$$\mathbf{P} = \langle \mathbf{P}_\mu \rangle, \tag{9}$$

and the microscopic equilibrium equation

$$\int_{\Omega_{\mathbf{Y}}} \mathbf{P}_\mu : (\nabla_{\mathbf{Y}}\, \mathrm{d}\mathbf{u}_\mu)\, \mathrm{d}V_\mu = 0, \qquad \forall\ \mathrm{d}\mathbf{u}_\mu \in \mathcal{V}_{\mathbf{u}_\mu}, \tag{10}$$

are direct consequences of the variational relation (6) (Blanco et al., 2014; de Souza Neto et al., 2015). It is important to note that the equilibrium equation (10) is conveniently written in terms of the variations of the microscopic displacements field $\mathrm{d}\mathbf{u}_\mu$, rather than the fluctuations $\mathrm{d}\tilde{\mathbf{u}}_\mu$ as shown in de Souza Neto et al. (2015).

2.1.3. Incremental microscopic equilibrium based on a minimum principle

The mechanical equilibrium of the microscale can be obtained from the minimum principle

$$(\mathbf{u}_{\mu_{n+1}})^{\text{opt}} = \arg \inf_{\mathbf{u}_{\mu_{n+1}} \in \mathcal{K}_{\mathbf{u}_\mu}} \Psi, \qquad \Psi \overset{\text{def}}{=} \langle \mathcal{P}_\mu \rangle, \tag{11}$$

where $\Psi(\mathbf{F}_{n+1})$ is a macroscopic potential defined as the volumetric average of the microscopic incremental potential $\mathcal{P}_\mu$ used in variational constitutive approaches (see Ortiz and Stainier (1999) and Radovitzky and Ortiz (1999) for further details on variational constitutive modeling). In view this constitutive theory, the potential $\mathcal{P}_\mu$ assumes the form of the Helmholtz free energy ψ if a classical hyperelastic behavior is considered, i.e., $\mathcal{P}_\mu = \psi$.

Taking into account the principle (11), it is easy to show that the stationarity condition of the potential Ψ - by means of the Gateaux derivative - results in the incremental version of the equilibrium equation (10), where further details can be found in Miehe (2003). Moreover, the minimum principle (11) provides a convenient numerical framework to solve the equilibrium equations. Accordingly, the kinematic constraints $\mathcal{K}_{\mathbf{u}_\mu}$ can be considered into the problem by different optimization strategies, such as the Lagrange multiplier methods, for example.

The present numerical strategy was employed in this work to formulate and solve the microscopic equilibrium problem within a conventional nonlinear finite element framework, where further details will be presented in Section 2.2.2.

2.2. Multiscale approach for materials composed of helical fibers

The main objective of this work is to propose and investigate a multiscale boundary condition suitable to represent the multiscale mechanics of RVEs reinforced with helical fibers (similar to that shown in Figure 1). Moreover, focus will be given to macroscopic loadings aligned axially and transversely to helical fibers. However, the numerical analysis of this class of RVEs under such conditions is not straightforward due to a couple of issues that are discussed below.

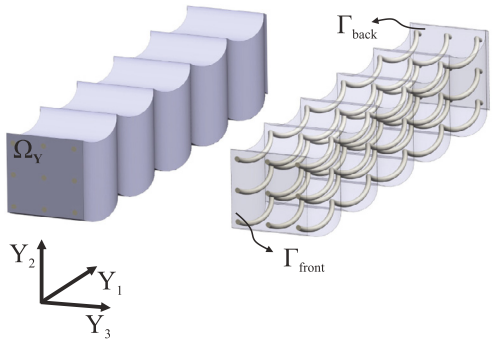

Fig. 1. Illustration of an RVE of a material composed of helical fibers embedded in a matrix.

1. On the one hand, the linear boundary displacements model imposes considerable constraints on the kinematics of the RVE, overestimating the deformation of the matrix. On the other hand, the minimally constrained model leads to heavily deformed mesh patterns when the RVE undergoes finite macroscopic deformations (see Figure 4).
2. Simple RVEs with straight boundary surfaces that account for the important continuity of the helical fibers are unlikely to be designed. Therefore, unusual helical (wavy-like) boundary surfaces are required to account for the geometric characteristics of these RVEs (see Figures 1 and 2d).
3. Even if the geometry of the RVE was designed to be a periodic partition of the three-dimensional medium, their unusual boundary surfaces preclude the use of standard techniques to enforce the periodic boundary conditions in a strong manner. This issue is related with the mesh generation, which must be able to provide a consistent one-to-one mapping between nodes of the periodic boundaries. On the other hand, weak approaches could be employed instead (Nguyen et al., 2012). However, the numerical implementation of such approaches into a conventional nonlinear finite element code is cumbersome.

In view of the issues listed above, one can note that the classical multiscale boundary conditions, i.e., the linear, periodic and minimal models, seem not to be suitable choices for the class of RVEs discussed herein. Therefore, new types of boundary conditions are required in this case.

As pointed out in Section 2.1.2, any space $\mathcal{K}_{\mathbf{u}_\mu} \subset \mathcal{K}^{\min}_{\mathbf{u}_\mu}$ that fulfills the variational statement (6) is kinematically admissible. In other words, a broad range of microstructural boundary conditions can be proposed in view of the present multiscale theory. Among them, the so-called mixed multiscale boundary conditions arise as a convenient option to overcome the drawbacks previously discussed. Generally, these boundary conditions mix two types of the classical ones, where several combinations are possible (Hazanov and Amieur, 1995; Pahr and Zysset, 2008; Mercer et al., 2015). Particularly, those that combine the linear boundary displacements model with the minimally constrained model will be investigated in this work, where further details are discussed in the next section.

2.2.1. The proposed multiscale boundary conditions

The sketch shown in Figure 1 illustrates an RVE composed of helical fibers embedded in a matrix. The helical fibers are preferentially aligned in the direction Y_1 and the boundary surfaces Γ_{front} and Γ_{back} are oriented transversely to them. It is important to mention that the boundaries Γ_{front} and Γ_{back} need not necessarily be straight planes or perpendicular to the direction Y_1. Moreover, in the present formulation, the lateral boundaries of the RVE are not restricted to any particular layout.

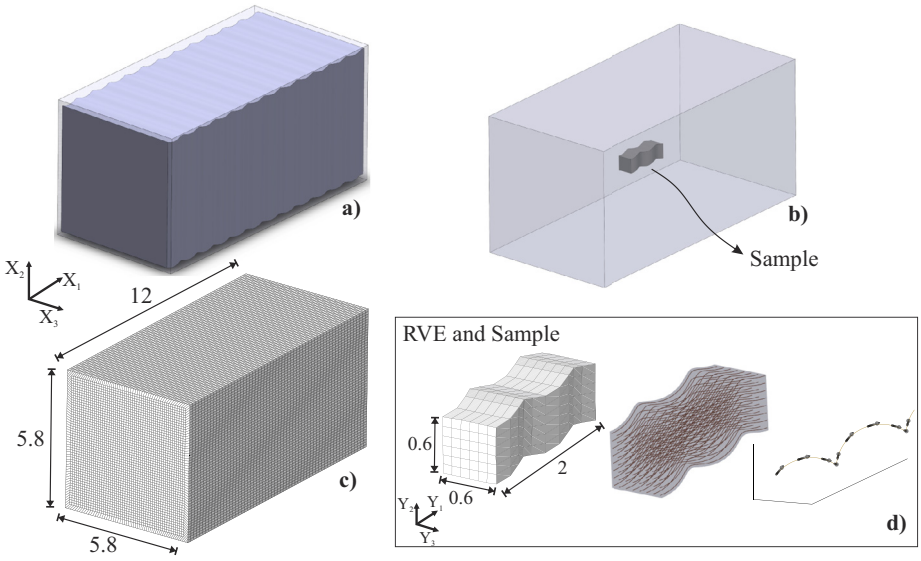

Fig. 2. Geometry of the numerical specimen of a composite material reinforced with helical fibers. (a) Inner region shape designed to follow the helical geometry of fibers. (b) Sketch emphasizing the sample located in the centroid of the specimen. (c) View of the external finite element mesh and dimensions of the numerical specimen. (d) Geometry, finite element mesh and dimensions of the sample and RVE. Illustrative representation of the parallel distribution of the helical fibers. The black arrows represent the local directions of fibers following the tangent of the helical equation (unit vectors $\mathbf{m}_{\mathbf{Y}}$).

In view of this class of RVEs, two mixed types of multiscale boundary conditions are suggested, both of them allying characteristics of the linear boundary displacements model and the minimally constrained model.

The first multiscale boundary condition investigated is called herein the *Mixed Linear Minimal Model* (MLM), which is denoted by

$$\mathcal{K}^{\mathrm{MLM}}_{\mathbf{u}_\mu} \overset{\mathrm{def}}{=} \left\{ \mathbf{u}_\mu \in \mathcal{K}^{\mathrm{min}}_{\mathbf{u}_\mu} \,\middle|\, \mathbf{u}_\mu = (\nabla_{\mathbf{X}}\mathbf{u})\mathbf{Y};\quad \forall\ \mathbf{Y} \in \hat{\Gamma} \right\}. \tag{12}$$

where $\hat{\Gamma} \overset{\mathrm{def}}{=} \Gamma_{\mathrm{front}} \cup \Gamma_{\mathrm{back}}$. One can see from the space (12) that the microscopic displacements resulting from the linear boundary displacements model are imposed only on boundaries Γ_{front} and Γ_{back}. This proposition aims to deal with the drawback related to the heavily deformed mesh patterns resulting from the minimally constrained model (see item 1 of the previous section). Moreover, in order to avoid further restrictions on the kinematic of the RVE, the remaining degrees of freedom are treated by the minimally constrained model.

The second boundary condition proposed arises from a slightly, but important, modification on the space (12). In this case, only the contribution $(\mathbf{u}_\mu)_1$ of the linear boundary displacements model, which is oriented axially to the helical fibers (see Figure 1), is imposed on boundaries Γ_{front} and Γ_{back}. This assumption leads to a kinematically admissible space, namely, the *Mixed Axial-Linear Minimal Model* (MALM), which is formally defined as

$$\mathcal{K}^{\mathrm{MALM}}_{\mathbf{u}_\mu} \overset{\mathrm{def}}{=} \left\{ \mathbf{u}_\mu \in \mathcal{K}^{\mathrm{min}}_{\mathbf{u}_\mu} \,\middle|\, (\mathbf{u}_\mu)_1 = [(\nabla_{\mathbf{X}}\mathbf{u})\mathbf{Y}]_1;\ \forall\ \mathbf{Y} \in \hat{\Gamma} \right\}. \tag{13}$$

It is important to note that in the space (13), the transverse microscopic displacements $(\mathbf{u}_\mu)_2$ and $(\mathbf{u}_\mu)_3$ on $\hat{\Gamma}$ must respect the minimally constrained model. Therefore, one can verify that $\mathcal{K}^{\mathrm{MLM}}_{\mathbf{u}_\mu}$ is a more restricted space than $\mathcal{K}^{\mathrm{MALM}}_{\mathbf{u}_\mu}$.

2.2.2. Solution strategy

The solution of the microstructural equilibrium is guided by the incremental approach discussed in Section 2.1.3. Therefore, the proposed models $\mathcal{K}^{\mathrm{MLM}}_{\mathbf{u}_\mu}$ or $\mathcal{K}^{\mathrm{MALM}}_{\mathbf{u}_\mu}$ are considered into the equilibrium through the following numerical strategy.

- Firstly, the kinematic constraints related to the minimal space $\mathcal{K}^{\mathrm{min}}_{\mathbf{u}_\mu}$ are enforced by the Lagrange multiplier method in the minimum principle (11), which in turns is formulated to be solved by the classical Newton's procedure.
- Secondly, after the finite element discretization, the prescribed displacements resulting from the linear boundary displacements model defined in $\mathcal{K}^{\mathrm{MLM}}_{\mathbf{u}_\mu}$ or $\mathcal{K}^{\mathrm{MALM}}_{\mathbf{u}_\mu}$ are imposed in the respectively degrees of freedom of the nodes belonging to the boundary $\hat{\Gamma}$.

The strategies listed above are briefly detailed in the sequence. In view of the minimum principle (11), the kinematic constraints defined in $\mathcal{K}^{\mathrm{min}}_{\mathbf{u}_\mu}$ (see Equation (3)) are taken into account by means of the Lagrangian functional

$$\begin{aligned}\mathcal{L}(\mathbf{x}_{n+1}) \overset{\mathrm{def}}{=}\ & \langle \mathcal{P}^{\mathrm{red}}_{\mathrm{inc}} \rangle + \boldsymbol{\Lambda}_{n+1} : (\mathbf{F}_{n+1} - \langle \mathbf{F}_{\mu_{n+1}} \rangle) \\ & - \boldsymbol{\gamma}_{n+1} \cdot \langle \mathbf{u}_{\mu_{n+1}} \rangle,\end{aligned} \tag{14}$$

where $\mathbf{x}_{n+1} \overset{\mathrm{def}}{=} \{\mathbf{u}_{\mu_{n+1}}, \boldsymbol{\Lambda}_{n+1}, \boldsymbol{\gamma}_{n+1}\}$ is the set of unknown variables. The second order tensor $\boldsymbol{\Lambda}_{n+1}$ and the vector $\boldsymbol{\gamma}_{n+1}$ are the Lagrange multipliers. Consequently, the minimum principle (11) is replaced by the unconstrained optimization problem

$$(\mathbf{x}_{n+1})^{\mathrm{opt}} = \arg \underset{\mathbf{x}_{n+1}}{\mathrm{stat}}\ \mathcal{L}(\mathbf{x}_{n+1}). \tag{15}$$

The variational principle (15) is formulated to be solved by the classical Newton's procedure and the resulting nonlinear equations are discretized by the standard finite element method (further operational details are shown in the appendices). Accordingly, a state related to a current iteration $(k+1)$ of the Newton-Raphson algorithm is updated by

$$\underline{\mathbf{K}}^{(k)}_{\mathrm{T}_{n+1}} \underline{\Delta \mathbf{x}}_{n+1} = -\underline{\mathbf{r}}^{(k)}_{n+1}, \qquad \underline{\mathbf{x}}^{(k+1)}_{n+1} = \underline{\mathbf{x}}^{(k)}_{n+1} + \underline{\Delta \mathbf{x}}_{n+1}, \tag{16}$$

where $\underline{\mathbf{x}}^{\mathrm{T}} \overset{\mathrm{def}}{=} [\underline{\mathbf{q}}^{\mathrm{T}} \ \underline{\boldsymbol{\Lambda}}^{\mathrm{T}} \ \underline{\boldsymbol{\gamma}}^{\mathrm{T}}]$ is the vector containing the nodal microscopic displacements $\underline{\mathbf{q}}$ and the Lagrange multipliers. The specific forms for the residual vector $\underline{\mathbf{r}}$ and the tangent matrix $\underline{\mathbf{K}}_{\mathrm{T}}$ are provided in Appendix B. The underlined variables $\underline{(\cdot)}$ are arranged into a compact matrix notation (Voigt mapping) generally used in finite element codes (see Jog, 2007).

Finally, the prescribed displacements resulting from the linear boundary displacements model defined in $\mathcal{K}^{\mathrm{MLM}}_{\mathbf{u}_\mu}$ or $\mathcal{K}^{\mathrm{MALM}}_{\mathbf{u}_\mu}$ are enforced in the degrees of freedom of the nodes belonging to the boundary $\hat{\Gamma}$ into the linear system (16).

Regarding to numerical implementation, it is important to mention that the models $\mathcal{K}^{\mathrm{MLM}}_{\mathbf{u}_\mu}$ and $\mathcal{K}^{\mathrm{MALM}}_{\mathbf{u}_\mu}$, in contrast to the periodic boundary condition, do not require particular mappings nor additional algorithmic handling.

2.3. Verification of the multiscale approach

One of the difficulties to assess the effectiveness of an RVE-based homogenization procedure is the availability of a reference solution. A possible one can be obtained by performing a numerical test on a specimen sufficiently large in comparison to the size of the RVE. The solution fields found at the inner part of the specimen are expected to be representative of what should be obtained on the RVE when submitted to appropriate homogenization procedures. This approach is explored in the sequence.

2.3.1. The constitutive model

Aiming at multiscale investigations of tendon tissues, one considers a hypothetical material bioinspired by the microstructure of tendon fascicles. Briefly, tendon fascicles are mainly composed of helical arrangements of bundles of collagen fibrils, called collagen fibers, embedded in a cellular matrix (tenocytes) (Kalson et al., 2015). Based on this morphology, the material considered in present study is composed of an isotropic matrix reinforced with helical fibers. In order to keep the simplicity of the proposed verification strategy, the matrix and fibers are modeled by a fiber-reinforced hyperelastic model. This model is based on the fourth invariant $I_4 \overset{\text{def}}{=} \mathbf{C}\colon \mathbf{A_Y} = (\lambda_f)^2$, where $\mathbf{C} \overset{\text{def}}{=} \mathbf{F}^T\mathbf{F}$ is the right Cauchy-Green tensor, λ_f is the stretch of fibers that respect the mapping $\lambda_f \mathbf{m_y} = \mathbf{F}\mathbf{m_Y}$ and $\mathbf{A_Y} \overset{\text{def}}{=} \mathbf{m_Y} \otimes \mathbf{m_Y}$ is the so-called structural tensor. The unit vectors $\mathbf{m_Y}$ and $\mathbf{m_y}$ represent the local directions of the helical fibers in the referential and spatial configuration, respectively. Such models are well established in the literature and further details can be found elsewhere (Schröder and Neff, 2003; Ehret and Itskov, 2007; Holzapfel and Ogden, 2009).

In view of this invariant-based constitutive theory, the following strain energy is used:

$$\psi \overset{\text{def}}{=} \psi_m + \psi_f, \tag{17}$$

in which ψ_m is the isotropic contribution (generally assigned to the matrix or matrix/fibers interactions) and ψ_f is an additional energy associated to the stretch of fibers. In present modeling approach, the local vector bases $\mathbf{m_Y}$ are assumed to follow the tangents of the helical fibers (see the black arrows in Figure 2d). Accordingly, the contribution of the tensile response of fibers varies at each integration point of the finite element mesh, rendering to a non-homogeneous material distribution.

The response of the matrix is considered by the Neo-Hookean function

$$\psi_m \overset{\text{def}}{=} \frac{\mu}{2}[\text{tr}(\mathbf{C}) - 3] - \mu \ln(J) + \frac{\kappa}{2}[\ln(J)]^2, \tag{18}$$

where μ and κ are the constitutive constants and $J \overset{\text{def}}{=} \det(\mathbf{F})$ is the volumetric Jacobian. The fibers are modeled by the polynomial form

$$\psi_f \overset{\text{def}}{=} \begin{cases} 0 & \text{if} \quad 0 < \lambda_f < 1 \\ k_1(I_4 - 1)^2 + k_2(I_4 - 1)^3 & \text{if} \quad \lambda_f \geq 1 \end{cases}, \tag{19}$$

in which k_1 and k_2 are the material parameters. One can see in (19) that the mechanical response of fibers is activated only for tensile states.

In order to consider fibers stiffer than the matrix, the values of $\{\mu, \kappa, k_1, k_2\} = \{0.5, 5, 17, 585\} \times 10^3$ were assumed for the material constants.

2.3.2. The specimen and the proposed RVE

One considers a hexahedral numerical *specimen* (Figure 2) made of the material described in Section 2.3.1. The helical shape, although not classical, is suitable for structured hexahedral meshes. In order to achieve an appropriate balance between numerical costs and performance to accomplish the main objectives addressed in present investigation, low order 8-nodes linear elements were used.

Helical fibers have a crimp length of 1.0 and diameter of 0.1. Fibers are distributed parallel to one another and they are axially aligned in the direction X_1. This specimen contains three mesh regions. A first external mesh layer, with straight boundary surfaces (see the mesh of Figure 2c) surrounds a second internal mesh designed to follow the helical geometry of fibers (see the helical wavy-like pattern shown in the inner region of Figure 2a). The third region consist on a small *sample* located on the centroid of this specimen (see Figure 2b and 2d).

The proposed RVE is a separate mesh, outside the specimen, conceived to follow the exact geometry of the previously defined sample. In this way, both, sample and RVE shapes ensure the continuity of the helical fibers (this issue was highlighted in Section 2.2). Further details related to the geometry, mesh and distribution of fibers within the sample and RVE are depicted in Figure 2d. It is worth mentioning that, despite a smother geometry and discretization on the RVE could be used, specimen, sample and RVE share identical meshes, and thus numerical results are comparable in a consistent manner.

It is important to state that the RVE is composed of a single material phase, whose behavior depends locally on the directions of fibers (see Section 2.3.1). Since these directions change with the helical wavelength which is much smaller than the structural scale, the RVE thus comprises a non-homogeneous material distribution.

2.3.3. The numerical experiment on the specimen

The numerical experiment consists of a displacement-controlled monotonic triaxial test on the specimen shown in Figure 2. In order to keep the main loadings aligned axially and transversely to helical fibers, the specimen is subjected to an elongation of 20% in the direction X_1 and a compression of 6% in the directions X_2 and X_3. The prescribed displacements are assigned to the degrees of freedom perpendicular to the boundary surfaces while those transverse to the prescribed directions are allowed to deform freely.

The loadings of interest in fiber-reinforced materials are usually those aligned to the helical axis of fibers. According to this, the first Piola-Kirchhoff stress component $(\mathbf{P})_{11}$ that will be used as the reference value of the specimen is computed by the ratio between the resulting axial force and the undeformed cross section area of the specimen.

2.3.4. The numerical experiment on the RVE

Based on the boundary conditions imposed on the hexahedral specimen, the tensor

$$\mathbf{F} = \begin{bmatrix} \lambda_1 & 0 & 0 \\ 0 & \lambda_2 & 0 \\ 0 & 0 & \lambda_3 \end{bmatrix}, \tag{20}$$

with stretches $(\lambda_1, \lambda_2, \lambda_3) = (1.20, 0.94, 0.94)$ represents the homogenized deformation gradient to which the whole specimen is submitted. This tensor is then used as input data to perform the homogenization procedures described in Section 2.1 on the RVE of Figure 2d. Once these procedures are completed, the corresponding homogenized first Piola-Kirchhoff stress tensor is obtained directly from Equation (9).

3. Results

In order to verify how the kinematics of the RVE are affected by the multiscale boundary conditions, the deformation of the mesh and the von Mises measure of the logarithmic strain field on the RVE are compared to the corresponding fields observed on the sample (see Figure 3).

Similarly, Figure 4 compares the deformed meshes and von Mises strains obtained on the sample and RVE for a macroscopic axial stretch $\lambda_1 = 1.12$. It is important to mention that no solution was achieved with the minimally constrained model for macroscopic stretches beyond 1.12 due to excessive mesh deformation (see Figure 4e).

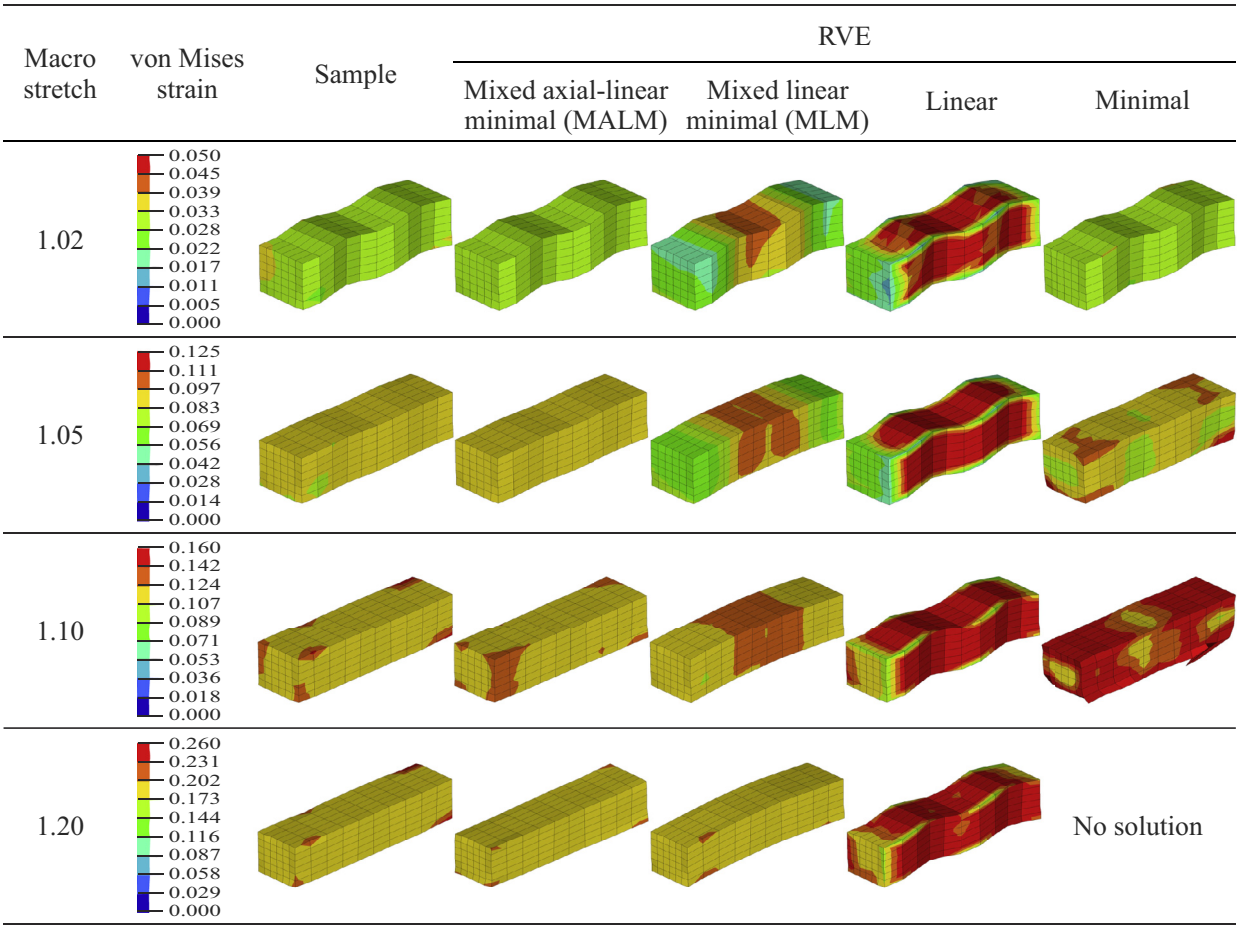

Fig. 3. von Mises measure of the logarithmic strain at the sample and the same field on the RVE for different multiscale boundary conditions. No solution was obtained with the minimally constrained model for a stretch beyond 1.12 due to high mesh deformation.

Figure 5 illustrates the evolution of the directions (arrows) and the stretch values of fibers λ_f at different stages of the macroscopic deformation in a lateral view of the RVE for the mixed-axial linear minimal model (MALM). The arrows represent the spatial base vectors $\mathbf{m}_y$.

Axial stress-stretch curves calculated from the specimen and those predicted from the homogenization procedures, for each of the multiscale boundary condition tested, are plotted in Figure 6a. Figure 6b displays the axial stress-stretch curves computed from the specimen and those predicted from the homogenization procedures with the MALM model for three sets of the material properties of fibers: *Prop.1* = $\{k_1 = 34, k_2 = 1170\} \times 10^3$; *Prop.2* = $\{k_1 = 17, k_2 = 585\} \times 10^3$; *Prop.3* = $\{k_1 = 8.5, k_2 = 292.5\} \times 10^3$. The set of parameters *Prop.2* is twice softer than the set *Prop.1* and twice stiffer than the set *Prop.3*. For these analyses, the material parameters of the matrix are kept fixed.

Figure 7 compares the axial component of the macroscopic stress $(\mathbf{P})_{11}$ with the transverse stresses $(\mathbf{P})_{22}$, $(\mathbf{P})_{33}$ for the mixed-axial linear minimal model (MALM). Due to the contrasting stiffness between the axial and the transverse stresses, Figure 7b emphasizes only the mechanical response of the transverse stresses.

4. Discussion

According to the mesh patterns and the strain fields shown in Figure 3, the following observations are pointed out.

Firstly, the MALM model is the one that provides the closest results to those of the sample for all the evaluated axial stretch amplitudes. The second best results are those of the MLM model. Although the equivalent strain fields obtained with this boundary condition present suitable distributions beyond $\lambda_1 = 1.10$, the shape of the deformed mesh are slightly different from those of the sample (see the bow-like shape of the mesh depicted in Figure 4c). These results show that, while the space $\mathcal{K}^{\mathrm{MLM}}_{\mathbf{u}_\mu}$ over-restricts the RVE, the linear constraint on the single axial displacement component defined in the space $\mathcal{K}^{\mathrm{MALM}}_{\mathbf{u}_\mu}$ releases the RVE to find a better deformed configuration.

Following the same reasoning, the linear boundary displacements model provides worse results than previous ones. Since it imposes a linear deformation pattern to all nodes belonging to the boundaries of the RVE (see Figure 3 and 4d), this model overestimates the local strains on the matrix due to the uncoiling of fibers within the RVE. Finally, the minimally constrained model provides reasonable results for stretches up to $\lambda_1 = 1.05$. However, when the RVE undergoes macroscopic axial stretches larger than $\lambda_1 = 1.05$, heavily deformed mesh patterns are verified, as shown in Figure 3 and detailed in Figure 4e. In the present case, the finite element analysis fails to converge at $\lambda_1 = 1.12$. The failure of the numerical analysis is due to the excessive mesh deformation (see the bottom elements of Figure 4e), leading to ill-conditioning of the tangent matrix (poor representation of the Jacobian matrix), which in turns strongly affects the convergence of the Newton's procedure. It is worth to mention that similar mesh behavior (heavily deformed) was also reported by Miehe et al. (2002) for this particular boundary condition.

Comparing Figures 3 and 5 for the MALM model, one can see that, up to a global stretch $\lambda_1 = 1.05$, fibers do not exceed local stretches of $\lambda_f = 1.004$ (0.4% of strain). On the other hand, the matrix experiences (equivalent) strains of ~10%. This observation reinforces the known

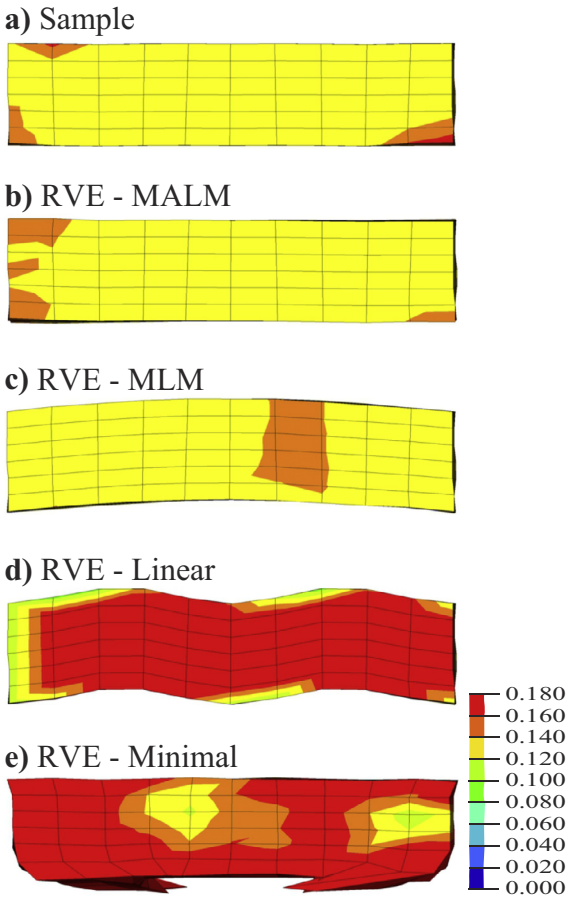

Fig. 4. Lateral views emphasizing the mesh deformation and the von Mises logarithmic strain at the macroscopic stretch of 1.12.

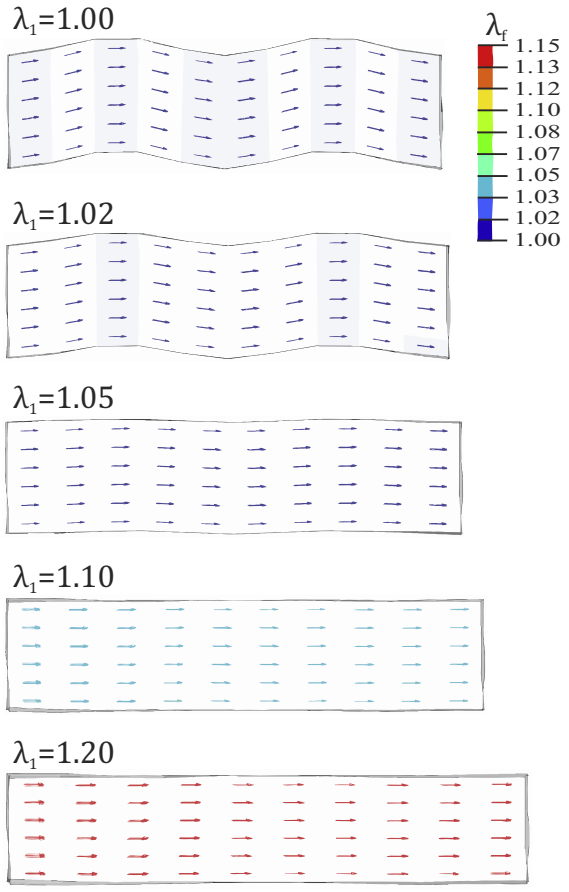

Fig. 5. Lateral views of the RVE showing the evolution of the axial directions (arrows) and stretch values of fibers within the RVE for the mixed-axial linear minimal model (MALM).

concept that during the initial macroscopic stretch stages, fibers are not intrinsically stretching, but uncoiling their helical structure. This fact is directly related to the shape of the homogenized stress-stretch curves. As can be seen in Figure 6a, a low stiffness is verified at the beginning of the curves (up to $\lambda_1 = 1.05$), behavior that is mainly ruled by the matrix. Beyond $\lambda_1 = 1.05$, an increasing of stiffness is verified due to stretching of fibers (compare Figure 5 and 6a). This particular macroscopic behavior is usually observed in experimental tensile tests on tendon fascicles, since this RVE was bioinspired by this tissue (Haraldsson et al., 2005; Legerlotz et al., 2010; Svensson et al., 2010).

One can see in Figure 6a that the MALM model was able to accurately predict the stress-stretch response of the specimen. The MLM model, on the other hand, slightly overestimates the stiffness of the referential curve. Similar behavior is also observed from the linear boundary displacements model. The minimally constrained model results in a softer response and, as comment earlier, it fails to converge at $\lambda_1 = 1.12$.

At this point an important issue must be highlighted. Despite both MLM and linear models present relatively good behaviors for the homogenized stress-stretch curves, they do not satisfactorily predict the local kinematics of the RVE. These differences are of major importance when the focus of the model is not its macroscopic output (stress-strain curves) but the local strain and stress fields among the composite constituents.

In order to investigate the sensitivity of the homogenization procedure regarding the stiffness of fibers, Figure 6b displays the homogenized stress-stretch curves computed from the specimen and those predicted from the homogenization procedures with the MALM model for three sets of the material properties of fibers. From these analyses one can verify that the mechanical response of fibers rules the macroscopic stress-stretch behavior, since fibers were considered much stiffer than the matrix. Moreover, the homogenized results retrieved from the MALM model still present good agreement with the reference solutions obtained from the specimen.

Another important issue for discussion concerns the homogenized transverse stress-stretch curves plotted in Figure 7; they let clear that the proposed tests do not represent a one-dimensional macroscopic stress state. This is a direct consequence of imposing an *a priori* transverse stretch in (20), related to a macroscopic Poisson's ratio $\nu = -(\lambda_2 - 1)/(\lambda_1 - 1) = -(\lambda_3 - 1)/(\lambda_1 - 1) = 0.3$ (see Section 2.3.4). Since achieved homogenized transverse stresses are positive (see Figure 7b), a Poisson ratio greater than $\nu = 0.3$ should be imposed to reduce their values. Moreover, a direct consistent way to achieve null transverse stresses is tailoring mixed multiscale models that combine strain-driven homogenized boundary conditions (like the present case) with stress-driven ones. For example, an efficient approach consists of embedding the macroscopic uniaxial stress constraint (stress-driven) and an appropriated kinematic constraint (strain-driven) within the variational principle (11). This is subject of further developments focusing on biological fibrous materials.

As have been pointed out throughout the manuscript, a practical application of the present computational homogenization approach concerns multiscale analyses of tendon fascicles. At this tissue scale, helical arrangements of collagen fibers embedded in a cellular matrix are found. Due to the complex geometrical and mechanical interactions between the load-bearing structures (fibers) with the cellular material

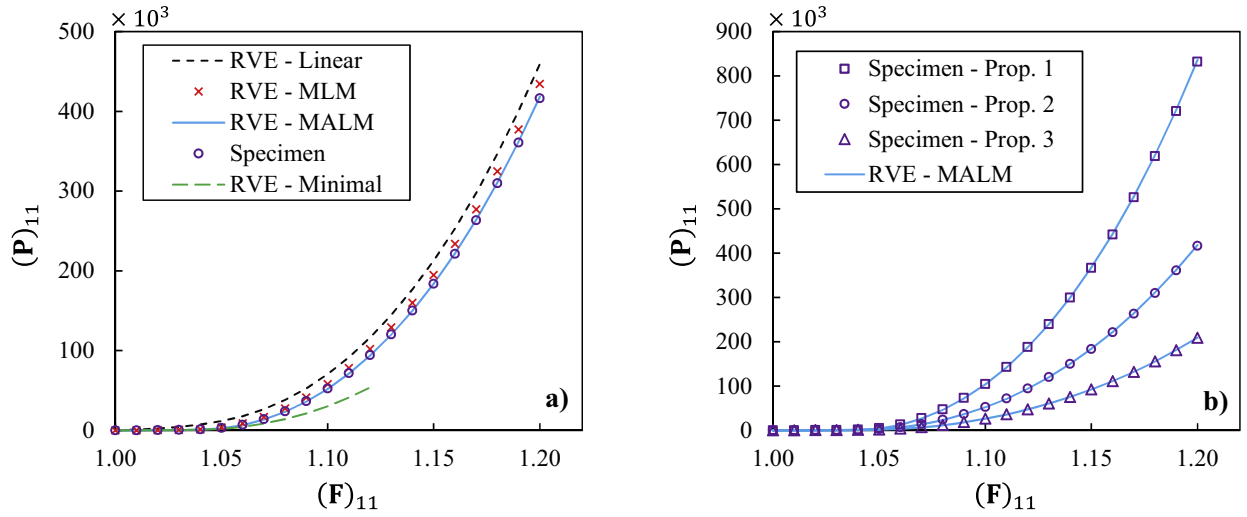

Fig. 6. (a) Comparison between the stress-stretch curves computed from the specimen with those predicted from the homogenization procedure for different multiscale boundary conditions. The numerical analysis with the minimally constrained model fails for macroscopic stretches beyond 1.12. (b) Stress-stretch curves computed from the specimen with those predicted from the homogenization procedure with the MALM model when the material parameters of fibers take values twice stiffer (Prop. 1) and twice softer (Prop. 3) than those used in (a) (Prop. 2).

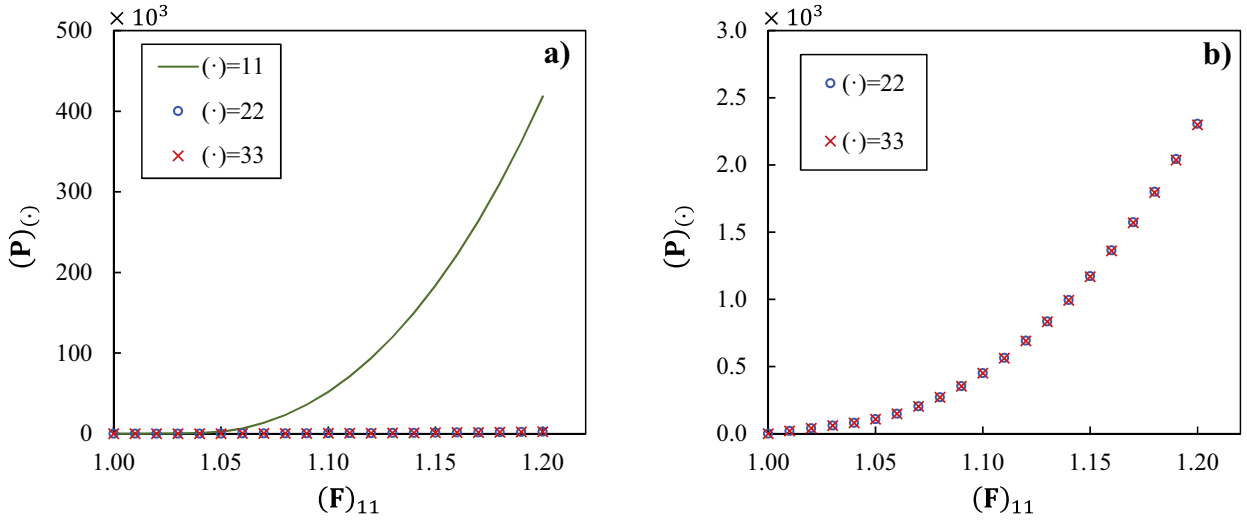

Fig. 7. Homogenized stress-stretch curves for the mixed-axial linear minimal model (MALM) emphasizing the contrasting stiffness between the axial stress component $(\mathbf{P})_{11}$ with the transverse stresses $(\mathbf{P})_{22}$ and $(\mathbf{P})_{33}$.

phase, unusual mechanical behaviors are observed. For example, tensile tests in tendon fascicles report Poisson's ratios ranging from 0.7 to 4, indicating volume reduction under tension (Cheng et al., 2007; Reese and Weiss, 2013). As discussed previously, the local kinematics of helical fibers under tensile states may lead to large Poisson's ratios. However, in what ways these large transverse strains affect the local kinematics of cells and induce physiological changes in tissue homeostasis, is still an open research issue. According to this, an appropriate numerical prediction of the deformation fields on the RVE is a first step to a better understanding on how the biomechanical environment affect the physiological behaviors of the tissue, investigating, for example, strain localization, local damage processes and mechanotransduction mechanisms (Wang, 2006; Lavagnino et al., 2015; Popov et al., 2015).

5. Conclusions

An RVE-based multiscale numerical approach for the finite strain analysis of materials composed of helical fibers embedded in a matrix was presented. An unusual helical (wavy-like) RVE was proposed bioinspired by the morphology of tendon fascicles to account for the important continuity of the helical fibers. Due to the unusual boundary geometry of the RVE, the numerical implementation of the periodic boundary displacements model within a conventional finite element code is cumbersome. Moreover, it was verified that the others classical boundary conditions, namely, the linear boundary displacements model and the minimally constrained model, seem not to be suitable choices for the multiscale analyses of this class of RVEs. As a consequence, two new models called *Mixed Linear Minimal Model* (MLM) and *Mixed Axial-Linear Minimal Model* (MALM) were proposed mixing appropriate features of the linear and minimally constrained boundary conditions.

A numerical strategy based on a displacement-controlled monotonic triaxial tests on specimens larger than the RVE served as a reference to validate the proposed models.

Results concerning microscopic strain fields and homogenized stress-stretch curves on the RVE point out the MALM model as the one that predicts with great accuracy not only the homogenized quantities but also the kinematic fields within the specimen.

Conflict of interest statement

The authors have no conflicts of interest to disclose.

Acknowledgments

The authors would like to thank the financial support provided by the Brazilian funding agencies CAPES - (Coordination for the Improvement of Higher Education Personnel) and CNPq - (National Council for Scientific and Technological Development).

Appendix A. Linearizations

A.1. Stationarity condition

The stationarity condition of the Lagrangian (14) is defined through the variation $\mathrm{d}\mathcal{L} = 0$, which results in the following nonlinear system of equations:

$$\begin{cases} \dfrac{\partial \mathcal{L}}{\partial \mathbf{u}_\mu}\cdot \mathrm{d}\mathbf{u}_\mu = & \langle \mathbf{P}_\mu \colon (\nabla_{\mathbf{Y}}\, \mathrm{d}\mathbf{u}_\mu)\rangle - \boldsymbol{\Lambda}\colon \langle \nabla_{\mathbf{Y}}\, \mathrm{d}\mathbf{u}_\mu\rangle \\ & - \boldsymbol{\gamma}\cdot\langle \mathrm{d}\mathbf{u}_\mu\rangle = 0 \\ \dfrac{\partial \mathcal{L}}{\partial \boldsymbol{\Lambda}}\colon \mathrm{d}\boldsymbol{\Lambda} = & \mathrm{d}\boldsymbol{\Lambda}\colon (\mathbf{F} - \langle \mathbf{F}_\mu\rangle) = 0 \\ \dfrac{\partial \mathcal{L}}{\partial \boldsymbol{\gamma}}\cdot \mathrm{d}\boldsymbol{\gamma} = & -\mathrm{d}\boldsymbol{\gamma}\cdot\langle \mathbf{u}_\mu\rangle = 0 \end{cases} \tag{A.1}$$

For the sake of clarity, the time-discrete notation $(\cdot)_{n+1}$ is not shown in the above variables and will be omitted henceforward.

A.2. Linearization of the equilibrium equations

The Newton-Raphson procedure requires the second variation of the Lagrangian $\mathcal{L}$. In this case, the Gateaux derivatives of (A.1) in the directions of the increments $\Delta\mathbf{u}_\mu$, $\Delta\boldsymbol{\Lambda}$ and $\Delta\gamma$ result in

$$\frac{\partial}{\partial \mathbf{u}_\mu}\left(\frac{\partial \mathcal{L}}{\partial \mathbf{u}_\mu}\cdot \mathrm{d}\mathbf{u}_\mu\right)\cdot\Delta\mathbf{u}_\mu = \langle (\nabla_{\mathbf{Y}}\, \mathrm{d}\mathbf{u}_\mu)\colon \mathbb{A}_\mu \colon (\nabla_{\mathbf{Y}}\, \Delta\mathbf{u}_\mu)\rangle, \tag{A.2}$$

$$\frac{\partial}{\partial \boldsymbol{\Lambda}}\left(\frac{\partial \mathcal{L}}{\partial \mathbf{u}_\mu}\cdot \mathrm{d}\mathbf{u}_\mu\right)\colon \Delta\boldsymbol{\Lambda} = -\langle \nabla_{\mathbf{Y}}\, \mathrm{d}\mathbf{u}_\mu\rangle\colon \Delta\boldsymbol{\Lambda}, \tag{A.3}$$

$$\frac{\partial}{\partial \boldsymbol{\gamma}}\left(\frac{\partial \mathcal{L}}{\partial \mathbf{u}_\mu}\cdot \mathrm{d}\mathbf{u}_\mu\right)\cdot\Delta\boldsymbol{\gamma} = -\langle \mathrm{d}\mathbf{u}_\mu\rangle\cdot\Delta\boldsymbol{\gamma}, \tag{A.4}$$

$$\frac{\partial}{\partial \mathbf{u}_\mu}\left(\frac{\partial \mathcal{L}}{\partial \boldsymbol{\Lambda}}\colon \mathrm{d}\boldsymbol{\Lambda}\right)\cdot\Delta\mathbf{u}_\mu = -\mathrm{d}\boldsymbol{\Lambda}\colon \langle \nabla_{\mathbf{Y}}\, \Delta\mathbf{u}_\mu\rangle, \tag{A.5}$$

$$\frac{\partial}{\partial \boldsymbol{\Lambda}}\left(\frac{\partial \mathcal{L}}{\partial \boldsymbol{\Lambda}}\colon \mathrm{d}\boldsymbol{\Lambda}\right)\colon \Delta\boldsymbol{\Lambda} = \frac{\partial}{\partial \boldsymbol{\gamma}}\left(\frac{\partial \mathcal{L}}{\partial \boldsymbol{\Lambda}}\colon \mathrm{d}\boldsymbol{\Lambda}\right)\cdot\Delta\boldsymbol{\gamma} = 0. \tag{A.6}$$

$$\frac{\partial}{\partial \mathbf{u}_\mu}\left(\frac{\partial \mathcal{L}}{\partial \boldsymbol{\gamma}}\cdot \mathrm{d}\boldsymbol{\gamma}\right)\cdot\Delta\mathbf{u}_\mu = -\mathrm{d}\boldsymbol{\gamma}\cdot\langle \Delta\mathbf{u}_\mu\rangle, \tag{A.7}$$

$$\frac{\partial}{\partial \boldsymbol{\Lambda}}\left(\frac{\partial \mathcal{L}}{\partial \boldsymbol{\gamma}}\cdot \mathrm{d}\boldsymbol{\gamma}\right)\colon \Delta\boldsymbol{\Lambda} = \frac{\partial}{\partial \boldsymbol{\gamma}}\left(\frac{\partial \mathcal{L}}{\partial \boldsymbol{\gamma}}\cdot \mathrm{d}\boldsymbol{\gamma}\right)\cdot\Delta\boldsymbol{\gamma} = 0. \tag{A.8}$$

The fourth order tensor $\mathbb{A}_\mu \overset{\text{def}}{=} \mathrm{d}\mathbf{P}_\mu/\mathrm{d}\mathbf{F}_\mu$ in (A.2) is the microscopic consistent tangent modulus (Simo and Taylor, 1985).

Appendix B. Numerical implementation

The underlined variables $\underline{(\cdot)}$ shown in this section are arranged into a compact matrix notation generally used in finite element codes (see Jog (2007) for further details on this topic).

B.1. Finite element discretization

Employing the standard finite element procedure (Bathe, 2006), the microscopic fields $\underline{\mathrm{d}\mathbf{u}_\mu}^{(e)}$ and $\underline{\Delta\mathbf{u}_\mu}^{(e)}$ and theirs respectively gradients $\underline{\nabla_{\mathbf{Y}}\, \mathrm{d}\mathbf{u}_\mu}^{(e)}$ and $\underline{\nabla_{\mathbf{Y}}\, \Delta\mathbf{u}_\mu}^{(e)}$ are approximated in a finite element (e) as follow:

$$\underline{\mathrm{d}\mathbf{u}_\mu}^{(e)} \approx \underline{\mathbf{N}}^{(e)}\underline{\mathrm{d}\mathbf{q}}^{(e)}, \quad \underline{\Delta\mathbf{u}_\mu}^{(e)} \approx \underline{\mathbf{N}}^{(e)}\underline{\Delta\mathbf{q}}^{(e)}, \tag{B.1}$$

$$\underline{\nabla_{\mathbf{Y}}\, \mathrm{d}\mathbf{u}_\mu}^{(e)} \approx \underline{\mathbf{G}}^{(e)}\underline{\mathrm{d}\mathbf{q}}^{(e)}, \quad \underline{\nabla_{\mathbf{Y}}\, \Delta\mathbf{u}_\mu}^{(e)} \approx \underline{\mathbf{G}}^{(e)}\underline{\Delta\mathbf{q}}^{(e)}, \tag{B.2}$$

where $\underline{\mathbf{q}}^{(e)^{\mathrm{T}}} = \left[\begin{array}{cccc} \underline{\mathbf{q}}_1^{(e)^{\mathrm{T}}} & \underline{\mathbf{q}}_2^{(e)^{\mathrm{T}}} & \cdots & \underline{\mathbf{q}}_n^{(e)^{\mathrm{T}}} \end{array}\right]$ is the nodal microscopic displacement vector and n is the number of nodes of the element. The matrices $\underline{\mathbf{N}}^{(e)}$ and $\underline{\mathbf{G}}^{(e)}$ contain the interpolation functions and their gradients, respectively.

B2. Residual and tangent matrix of the Newton-Raphson algorithm

Substitution of the approximations (B.1) and (B.2) into the nonlinear system (A.1) and its derivatives (A.2-A.8), leads to the residual vector

$$\underline{\mathbf{r}} \overset{\text{def}}{=} \left[\begin{array}{c} \underline{\mathbf{f}}_{\text{int}} - \underline{\mathbf{f}}_{\text{ext}} \\ V_\mu(\underline{\mathbf{F}} - \langle \underline{\mathbf{F}}_\mu \rangle) \\ V_\mu(\underline{\mathbf{u}} - \langle \underline{\mathbf{u}}_\mu \rangle) \end{array}\right], \tag{B.3}$$

and the tangent matrix

$$\underline{\mathbf{K}}_{\mathrm{T}} \overset{\text{def}}{=} \left[\begin{array}{ccc} \underline{\mathbf{K}} & -\underline{\mathbf{G}}^{\mathrm{T}} & -\underline{\mathbf{N}}^{\mathrm{T}} \\ -\underline{\mathbf{G}} & & \underline{\boldsymbol{\epsilon}} \\ -\underline{\mathbf{N}} & \underline{\boldsymbol{\epsilon}} & \end{array}\right], \tag{B.4}$$

respectively. In Equation (B.4) $\underline{\boldsymbol{\epsilon}}$ is a zero matrix. However, a perturbation is introduced in all elements of $\underline{\boldsymbol{\epsilon}}$ in order to avoid ill conditioning of the tangent matrix $\underline{\mathbf{K}}_{\mathrm{T}}$. In a double precision code, no numerical problems have been verified with $\underline{\boldsymbol{\epsilon}} = 10^{-14}$.

In equations (B.3) and (B.4) the following quantities are defined:

$$\underline{\mathbf{f}}_{\text{int}} \overset{\text{def}}{=} \overset{nel}{\underset{e=1}{\mathcal{A}}}\left[\int_{\Omega_{\mathbf{Y}}^{(e)}} \underline{\mathbf{G}}^{(e)^{\mathrm{T}}} \underline{\mathbf{P}}_\mu^{(e)} \mathrm{d}V_\mu^{(e)} \right], \tag{B.5}$$

$$\underline{\mathbf{f}}_{\text{ext}} \overset{\text{def}}{=} \underline{\mathbf{G}}^{\mathrm{T}} \underline{\boldsymbol{\Lambda}} + \underline{\mathbf{N}}^{\mathrm{T}} \underline{\boldsymbol{\gamma}}, \tag{B.6}$$

$$\underline{\mathbf{G}} \overset{\text{def}}{=} \overset{nel}{\underset{e=1}{\mathcal{A}}}\left[\int_{\Omega_{\mathbf{Y}}^{(e)}} \underline{\mathbf{G}}^{(e)} \mathrm{d}V_\mu^{(e)} \right], \tag{B.7}$$

$$\underline{\mathbf{N}} \overset{\text{def}}{=} \overset{nel}{\underset{e=1}{\mathcal{A}}}\left[\int_{\Omega_{\mathbf{Y}}^{(e)}} \underline{\mathbf{N}}^{(e)} \mathrm{d}V_\mu^{(e)} \right], \tag{B.8}$$

$$\underline{\mathbf{K}} \overset{\text{def}}{=} \overset{nel}{\underset{e=1}{\mathcal{A}}}\left[\int_{\Omega_{\mathbf{Y}}^{(e)}} \underline{\mathbf{G}}^{(e)^{\mathrm{T}}} \underline{\mathbb{A}}_\mu^{(e)} \underline{\mathbf{G}}^{(e)} \mathrm{d}V_\mu^{(e)} \right]. \tag{B.9}$$

where $\mathcal{A}$ is the finite element assembly operator. It is worth to mention that $\underline{\mathbf{f}}_{\text{int}}$ and $\underline{\mathbf{K}}$ are the same internal force vector and the stiffness matrix obtained from standard nonlinear finite element procedures.

References

Bathe, K., 2006. Finite Element Procedures. Pearson Education, Inc.

Bell, J.S., Hayes, S., Whitford, C., Sanchez-Weatherby, J., Shebanova, O., Vergari, C., Winlove, C.P., Terrill, N., Sorensen, T., Elsheikh, A., Meek, K.M., 2018. The hierarchical response of human corneal collagen to load. Acta Biomater. 65, 216–225.

Blanco, P.J., Sanchez, P.J., de Souza Neto, E.A., Feijo, R.A., 2014. Variational foundations and generalized unified theory of RVE-based multiscale models. Arch. Comput. Methods Eng. 23 (2), 191–253.

Cheng, V.W.T., Screen, H.R.C., 2007. The micro-structural strain response of tendon. J. Mater. Sci. 42 (21), 8957–8965.

Deng, J., Xu, Y., He, S., Chen, P., Bao, L., Hu, Y., Wang, B., Sun, X., Peng, H., 2017. Preparation of biomimetic hierarchically helical fiber actuators from carbon nanotubes. Nat. Protoc. 12 (7), 1349–1358.

Ehret, A.E., Itskov, M., 2007. A polyconvex hyperelastic model for fiber-reinforced materials in application to soft tissues. J. Mater. Sci. 42 (21), 8853–8863.

Frikha, A., Cartraud, P., Treyssède, F., 2013. Mechanical modeling of helical structures accounting for translational invariance. part 1: static behavior. Int. J. Solids Struct. 50 (9), 1373–1382.

Haraldsson, B.T., Aagaard, P., Krogsgaard, M., Alkjaer, M., Magnusson, S.P., 2005. Regoin-specific mechanical properties of the human patella tendon. J. Appl. Physiol. 98, 1006–1007.

Hazanov, S., Amieur, M., 1995. On overall properties of elastic heterogeneous bodies smaller than the representative volume. Int. J. Eng. Sci. 33 (9), 1289–1301.

Ho, R.M., Chiang, Y.W., Chen, C.K., Wang, H.W., Hasegawa, H., Akasaka, S., Thomas, E.L., Burger, C., Hsiao, B.S., 2009. Block copolymers with a twist. J. Am. Chem. Soc. 131 (51), 18533–18542.

Holzapfel, G.a., Ogden, R.W., 2009. Constitutive modelling of passive myocardium: a structurally based framework for material characterization. Philos. Trans. A Math. Phys. Eng. Sci. 367 (1902). 3445–75.

Huang, G., Mei, Y., 2015. Helices in micro-world: materials, properties, and applications. J. Mater. 1 (4), 296–306.

Jog, C., 2007. Foundations and Applications of Mechanics Volume I: Continuum Mechanics, 2nd Ed. I Alpha Science Intl Ltd.

Kalson, N.S., Lu, Y., Taylor, S.H., Starborg, T., Holmes, D.F., Kadler, K.E., 2015. A structure-based extracellular matrix expansion mechanism of fibrous tissue growth. 4. pp. 1–22.

Kravchenko, O.G., Qian, X., Kravchenko, S.G., Misiego, R., Pipes, R.B., Manas-Zloczower, I., 2017. Role of hierarchical morphology of helical carbon nanotube bundles on thermal expansion of polymer nanocomposites. J. Mater. Res. 32 (14), 2738–2746.

Lavagnino, M., Wall, M.E., Little, D., Banes, A.J., Guilak, F., Arnoczky, S.P., 2015. Tendon mechanobiology: current knowledge and future research opportunities. J. Orthop. Res. 33 (6), 813–822.

Legerlotz, K., Riley, G.P., Screen, H.R.C., 2010. Specimen dimensions influence the measurement of material properties in tendon fascicles. J. Biomech. 43 (12), 2274–2280.

Mercer, B.S., Mandadapu, K.K., Papadopoulos, P., 2015. Novel formulations of microscopic boundary-value problems in continuous multiscale finite element methods. Computer Methods in Applied Mechanics and Engineering. 286. pp. 268–292.

Messager, T., Cartraud, P., 2008. Homogenization of helical beam-like structures: application to single-walled carbon nanotubes. Comput. Mech. 41 (2), 335–346.

Miehe, C., 2003. Computational micro-to-macro transitions for discretized micro-structures of heterogeneous materials at finite strains based on the minimization of averaged incremental energy. Comput. Methods Appl. Mech. Eng. 192 (5–6), 559–591.

Miehe, C., Schotte, J., Lambrecht, M., 2002. Homogenization of inelastic solid materials at finite strains based on incremental minimization principles. application to the texture analysis of polycrystals. J. Mech. Phys. Solids 50 (10), 2123–2167.

Nguyen, V.D., Béchet, E., Geuzaine, C., Noels, L., 2012. Imposing periodic boundary condition on arbitrary meshes by polynomial interpolation. Comput. Mater. Sci. 55, 390–406.

Ortiz, M., Stainier, L., 1999. The variational formulation of viscoplastic constitutive updates. Comput. Methods Appl. Mech. Eng. 7825 (98), 419–444.

Pahr, D.H., Zysset, P.K., 2008. Influence of boundary conditions on computed apparent elastic properties of cancellous bone. Biomech. Model Mechanobiol. 7 (6), 463–476.

Palombini, F.L., Kindlein, W., de Oliveira, B.F., de Araujo Mariath, J.E., 2016. Bionics and design: 3d microstructural characterization and numerical analysis of bamboo based on x-ray microtomography. Mater. Charact. 120, 357–368.

Popov, C., Burggraf, M., Kreja, L., Ignatius, A., Schieker, M., Docheva, D., 2015. Mechanical stimulation of human tendon stem/progenitor cells results in upregulation of matrix proteins, integrins and MMPs, and activation of p38 and ERK1/2

kinases. BMC Mol. Biol. 16 (1), 6.
Radovitzky, R., Ortiz, M., 1999. Error estimation and adaptive meshing in strongly nonlinear dynamic problems. Comput. Methods Appl. Mech. Eng. 172 (1–4), 203–240.
Raghubanshi, H., Dikio, E.D., Naidoo, E.B., 2016. The properties and applications of helical carbon fibers and related materials: a review. J. Ind. Eng. Chem. 44, 23–42.
Reese, S.P., Weiss, J.a., 2013. Tendon fascicles exhibit a linear correlation between Poisson's ratio and force during uniaxial stress relaxation. J. Biomech. Eng. 135 (3), 34501.
Saeb, S., Steinmann, P., Javili, A., 2016. Aspects of computational homogenization at finite deformations: a unifying review from Reuss' to Voigt's bound. Appl. Mech. Rev. 68 (5).
Sanchez, C., Arribart, H., Guille, M.M.G., 2005. Biomimetism and bioinspiration as tools for the design of innovative materials and systems. Nat. Mater. 4 (4), 277–288.
Schröder, J., Neff, P., 2003. Invariant formulaiton of hyperelastic transverse isotropy based on polyconvex free energy functions. Int. J. Solids Struct. 40 (2), 401–445.
Simo, J., Taylor, R., 1985. Consistent tangent operators for rate-independent elastoplasticity. Comput. Methods Appl. Mech. Eng. 48 (1), 101–118.
de Souza Neto, E., Blanco, P., Sánchez, P., Feijóo, R., 2015. An RVE-based multiscale theory of solids with micro-scale inertia and body force effects. Mech. Mater. 80, 136–144.
Svensson, R.B., Hassenkam, T., Grant, C.A., Magnusson, S.P., 2010. Tensile properties of human collagen fibrils and fascicles are insensitive to environmental salts. Biophys. J. 99 (12), 4020–4027.
Wang, J.H.C., 2006. Mechanobiology of tendon. J. Biomech. 39 (9), 1563–1582.
Wang, L., Cui, Y., Qin, Q., Wang, H., Wang, J., 2016. Helical fiber pull-out in biological materials. Acta Mech. Solida Sin. 29 (3), 245–256.
Yashima, E., 2010. Synthesis and structure determination of helical polymers. Polym. J. 42 (1), 3–16.
Zhang, C., Mcadams, D.A., Grunlan, J.C., 2016. Correction to: nano/micro-manufacturing of bioinspired materials: a review of methods to mimic natural structures (adv. mater., (2016), 28, (6292), 10.1002/adma.201505555). Adv. Mater. 28 (39), 8566.